Check for updates

JGR Oceans

RESEARCH ARTICLE
10.1029/2023JC020627

The Response of the Upper Ocean to Tropical Cyclones in the South Pacific

Chao Han[1], **Melissa Bowen**[1], **and Philip Sutton**[2]

[1]School of Environment, University of Auckland, Auckland, New Zealand, [2]National Institute of Water and Atmospheric Research (NIWA), Wellington, New Zealand

Key Points:

- We develop an improved method to analyze Argo profile data to measure ocean temperature and salinity changes due to passages of tropical cyclones
- Upper ocean overturning is observed across the track of a tropical cyclone, with stronger upwelling on the left side and strongest upwelling below the center
- Upper ocean changes are correlated with the Local Wind Power Dissipation of the tropical cyclone and the ocean Cooling Inhibition Index

Supporting Information:

Supporting Information may be found in the online version of this article.

Correspondence to:

C. Han,
chao.han@auckland.ac.nz

Citation:

Han, C., Bowen, M., & Sutton, P. (2024). The response of the upper ocean to tropical cyclones in the South Pacific. *Journal of Geophysical Research: Oceans*, *129*, e2023JC020627. https://doi.org/10.1029/2023JC020627

Received 24 OCT 2023
Accepted 28 MAR 2024

Author Contributions:

Conceptualization: Chao Han, Melissa Bowen, Philip Sutton
Data curation: Chao Han, Melissa Bowen, Philip Sutton
Formal analysis: Chao Han
Funding acquisition: Melissa Bowen, Philip Sutton
Investigation: Chao Han
Methodology: Chao Han, Melissa Bowen
Project administration: Melissa Bowen
Resources: Chao Han
Software: Chao Han, Philip Sutton
Supervision: Melissa Bowen, Philip Sutton
Validation: Chao Han, Melissa Bowen
Visualization: Chao Han

© 2024 The Authors.
This is an open access article under the terms of the Creative Commons Attribution-NonCommercial License, which permits use, distribution and reproduction in any medium, provided the original work is properly cited and is not used for commercial purposes.

Abstract Consecutive Argo float profiles are used to observe upper ocean changes resulting from the passage of tropical cyclones (TCs) in the South Pacific between 2001 and 2023. Cross-sectional composites of the ocean response are produced by normalizing the distance between the profile and cyclone track by the 34-knot wind radius (R_{34}) of each TC to better resolve the average changes in water properties. Surface cooling in the initial mixed layer (ML) extends from the center to about twice R_{34} and is stronger to the left of the TC track. Subsurface warming at the base of the ML is observed between 0.4 and 2 R_{34} on both sides of the track. Strong cooling is observed in a distinct core directly under the TC path, reaching temperature changes of over −1.6°C between 70 and 450 m depth. Significant upwelling of over 40 m displacement is observed within ±0.05 R_{34}, extending to 1,000 m depth. Surface cooling (and subsurface warming at the base of the ML) are positively correlated with wind stress on the ocean from the TC, quantified by the Local Wind Power Dissipation (PD_L), and negatively correlated with the energy required to destratify the upper ocean, defined by a Cooling Inhibition index (CI). Subsurface warming is common with low CI but is not observed with high CI. We demonstrate an improved method to analyze Argo float data for measuring TC-upper ocean interaction in remote oceans and the usefulness of PD_L and CI in calibrating the TC-ocean interaction.

Plain Language Summary Tropical Cyclones, commonly known as Typhoons or Hurricanes, are formidable weather phenomena and they have a complex interaction with the upper ocean. Using data provided by an array of ocean-drifting floats known as the Argo Program, we examine the ocean's temperature and salinity response to Tropical Cyclones in the South Pacific. To scale for the different sizes of the Tropical Cyclones, we developed a method of scaling each float's location to the Cyclone's 34-knot wind radius. We have found significant cooling at the surface of the ocean and warming below the cooling layer in the top 100 m of the ocean. This is consistent with the theories of Cyclones overturning the upper ocean. This ocean response is stronger on the left side of the Cyclone's direction of travel. We also found significant upwelling below the cyclone's core region in the form of a deep cooling core extending to 1,000 m deep. We found there is a strong relationship between the upper ocean mixing and upwelling with the energy input to the upper ocean by the Cyclone, and the upper ocean's resistance to the cyclone mixing.

1. Introduction

Tropical Cyclones (TCs) play a major role in the air-sea heat exchange and modulation of the temperature-salinity structure of the upper ocean (Emanuel, 1986, 1988, 1991, 2003). TCs gain energy from the upper ocean mainly through latent heat flux (Park et al., 2011; Scoccimarro et al., 2011; Zedler et al., 2002), which increases with increasing SST (Emanuel, 1991, 1999b; Mainelli et al., 2008; Neetu et al., 2012). In return, TCs have long been observed to cause sea surface cooling (SSC): a cooler track along the ocean surface usually 0.5–1°C colder than the pre-TC Sea Surface Temperature (SST), strongest on the left (right) side of the TC track in the Southern (Northern) Hemisphere and over 100 km wide (Fisher, 1958; Vincent et al., 2013). After TC passage, the SSC wake is warmed by solar radiation, usually recovering to pre-TC level within 7–30 days (Guan et al., 2021; Hart et al., 2007; Pasquero & Emanuel, 2008; Wang et al., 2016).

Sea surface cooling results from both mixing and advection. Vertical mixing (sometimes called “heat pumping”) is the primary SSC mechanism of TCs weaker than Category 2 (defined as the maximum sustained wind speed, V_{max}, being less than 82 knots), changing the upper ocean during the TC passage (Huber & Sriver, 2007; Korty et al., 2008; Mei & Pasquero, 2013; Park et al., 2011). The stress and wave energy imparted to the surface ocean by the TC winds mix warmer, fresher water at the surface below the initial mixed layer (ML) and bring colder,

Writing – original draft: Chao Han
Writing – review & editing: Melissa Bowen, Philip Sutton

saltier water from below the ML, resulting in a deeper ML (Bond et al., 2011; Domingues et al., 2015; Huang et al., 2007; Liu et al., 2008; Zhang et al., 2021).

TCs stronger than Category 2 also generate SSC by vertical advection, bringing colder water upward to the surface (Mei et al., 2015). This process is sometimes called cold suction or Ekman suction. It occurs when the surface currents under the TC diverge, which is compensated for by deeper water moving upward. Water below the TC center is brought toward the surface by this localized upwelling and can displace the thermocline upward for hundreds of meters in depth (Scrosati, 2020; Zhang et al., 2016). Upwelling shoals the ML below the TC center, making it easier for surface mixing to penetrate the base of the ML (Huang et al., 2009; Potter et al., 2017). Surface water moves horizontally outward from the center, thickening the ML and causing downwelling at the outskirts of the TC thereby displacing the local thermocline downward (Hsu & Ho, 2019; Zhang et al., 2016).

The wind speed and translation speed of the TC are primary factors in the upper ocean changes. SSC increases with TC wind speed when V_{max} is below 95 knots but does not appear to increase when wind speed is above 95 knots (Mei & Pasquero, 2013; Mei et al., 2015; Park et al., 2011; Wu et al., 2007). Some studies suggest the SSC may be limited at higher winds due to the drag coefficient on the ocean surface (C_D) reaching a maximum and then dropping at higher wind speeds, reducing the transfer of energy into the ocean (Powell et al., 2003; Sanford et al., 2007; Zedler et al., 2009). The TC translation speed also controls the wind mixing strength with slower TCs usually generating more SSC than faster-moving ones with the same wind speed (Mei & Pasquero, 2013; Mei et al., 2015; Ni et al., 2021; Wu et al., 2007). Bister and Emanuel (1998) proposes a parameter called Wind Power Dissipation (PD) to estimate the total TC mechanical energy input to the upper ocean, accounting for both the TC wind speed and translation speed which is later improved in Emanuel (1999a, 2005). We have adapted this method in this study to calculate a Local Wind Power Dissipation (PD_L) to use with the ocean observations made at discrete locations.

The amount of SSC is also determined by how much energy is required to penetrate the stratified water at the base of the ML (Talley et al., 2011). An ocean with a deeper (shallower) ML or stronger (weaker) stratification at the ML base requires more (less) energy to mix into the stratified water at the base of the ML and produces a weaker (stronger) SSC (Domingues et al., 2015; Lin, Chen, et al., 2009; Lin et al., 2005, 2008; Liu et al., 2007; Maneesha et al., 2012; Mei et al., 2015; Neetu et al., 2012; Park et al., 2019; Zheng et al., 2008). As both stratification and mixed layer depth (MLD) enhance the upper ocean resistance to wind mixing, Vincent et al. (2012) proposed a parameter called the Cooling Inhibition index (CI) to combine these measures: CI is the cube root of the potential energy that would be required to mix below the ML and cool the sea surface to 2°C below the initial SST.

The TC-induced SSC can also in turn influence the TC intensity. The SSC changes the heat flux to the atmosphere and can weaken the TC intensity (Huang et al., 2015). Strong SSC can reduce TC intensity from its maximum obtainable intensity by up to 47% (Zhu & Zhang, 2006). If SSC is more than 2.5°C the TC can no longer intensify and will decay (Balaguru et al., 2014; Cione & Uhlhorn, 2003; Jaimes & Shay, 2009; Lin, Pun, & Wu, 2009; Lin et al., 2008; Lloyd & Vecchi, 2011; Pasquero & Emanuel, 2008; Yan et al., 2017). A stronger, slower-moving TC increases the TC-induced mixing, brings more subsurface cold water to the surface, causes more SSC, reduces heat flux to the atmosphere, and weakens. This atmosphere-ocean coupling demonstrates that TC-ocean interaction is important not only for ocean heat content change but also for predicting TC strength, especially in a future ocean that will likely be warmer and more stratified (Huang et al., 2015).

Ocean observations under TCs have been difficult to collect. Past studies primarily used ship-based observations (Fisher, 1958), data from gliders (Domingues et al., 2015; Glenn et al., 2016; Lim et al., 2020; Ni et al., 2021), and moorings (Black & Dickey, 2008; Bond et al., 2011; Girishkumar et al., 2014; Guan et al., 2021; Potter et al., 2017; Scrosati, 2020; Yang et al., 2015, 2019; Zelder et al., 2002, 2009; Zhang, Liu, et al., 2019). Data used for these methods are often limited in number and spatial coverage. The majority of these observations are near populated coastlines with fewer data in remote regions such as the South Pacific. Others have used satellite data to observe SST changes (Kobashi et al., 2019; Mei et al., 2015; Park et al., 2019; Wang et al., 2016; Zhang, Liu, et al., 2019), which provides sufficient spatial coverage but are hindered by the dense clouds associated with the TC blocking infrared radiation from the surface (Wentz et al., 2000) and the lack of subsurface and salinity data. Simulations of TCs (Price, 1981; Price et al., 1994; Zhang et al., 2018) provide valuable understanding but require observations for validation (Jacob & Koblinsky, 2007).

21699291, 2024, 4, Downloaded from https://agupubs.onlinelibrary.wiley.com/doi/10.1029/2023JC020627, Wiley Online Library on [18/06/2024]. See the Terms and Conditions (https://onlinelibrary.wiley.com/terms-and-conditions) on Wiley Online Library for rules of use; OA articles are governed by the applicable Creative Commons License

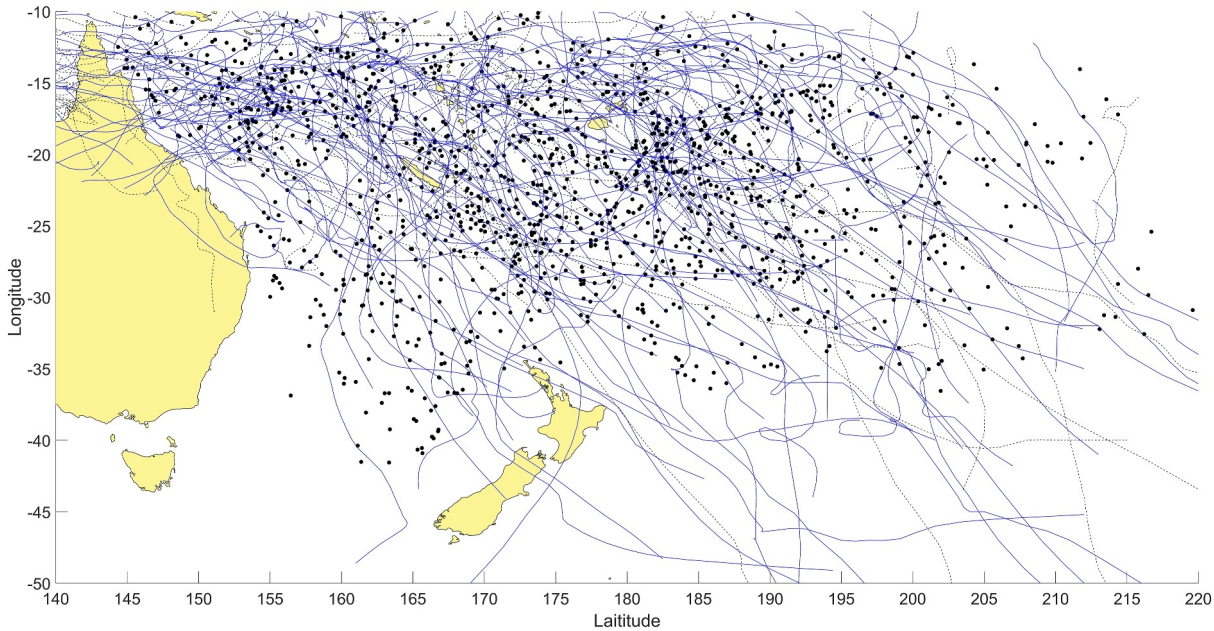

Figure 1. The tracks of all TCs (blue lines) in the South Pacific with locations of the post-TC Argo profiles used in this study and covering the period 2001/01/01–2023/07/01. The black dots are the locations of the post-TC Argo profiles after the passage of the TC. The dashed lines show TCs in the study period that had no Argo profile matches.

The Argo Program provides a unique source of subsurface data (Roemmich et al., 2019) that avoids many of the issues of other types of observations and has been used to investigate the upper ocean response to TCs. Several studies use Argo profiles pairs before and after the passage of a TC to analyze the ocean response in the Northwest Pacific (Baranowski et al., 2014; Liu et al., 2014; Park et al., 2011; Zhang et al., 2018). Cheng et al. (2015) averaged Argo profiles in all the ocean basins by their distance from the TC center and found that upper ocean cooling is more intense on the stronger side of the TC and cooling under the TC center extends hundreds of meters deep. Liu et al. (2007) and Lin et al. (2017) used a similar method, again averaging profile changes with distance. Wang et al. (2016) normalized cross-track location of the profile pairs with the 50-knot wind radius but only focused on the average TC-induced cooling cores in the Northwest Pacific. We improve on these previous methods to increase spatial resolution of the ocean response to TC from the Argo data.

With global warming, SST and TC intensity has increased over the past 35 years (Emanuel, 1987, 2005; Webster et al., 2005) and the increases are projected to continue (Balaguru et al., 2016; Emanuel et al., 2008; Held & Zhao, 2011; Kossin et al., 2020; Mann et al., 2006), prompting the need for better understanding of the interaction of TCs and the upper ocean (Emanuel, 2002; Huang et al., 2015; Mei et al., 2013; Sriver et al., 2010; Wang et al., 2014). This is especially true for the South Pacific which is relatively understudied compared to the Northern Hemisphere. Based on a previous study by Han (2023), this study utilized Argo data and improved methods to generate composite temperature and salinity responses to TCs. We then use the PD_L and CI parameters to gauge the TC and ocean controls on SSC. Section 2 introduces the methods. The following sections present and discuss the composite results in the South Pacific, including the cross-track temperature and salinity responses, the upwelling strength and the relationships with PD_L and CI. The results are then discussed and summarized in the final section.

2. Methods

2.1. Observations

To match the Argo observations with South Pacific TCs, the tracks of 237 TCs in the South Pacific between 2001/01/01–2023/07/01 were extracted from the International Best Track Archive for Climate Stewardship (IBTrACS) (Knapp et al., 2018). Each TC track contains location, maximum wind speed, the TC radius at 34, 50, and 64 knots at each quadrant (Northeast, Northwest, Southeast, Southwest), translation speed, and other variables every 3-hr.

21699291, 2024, 4, Downloaded from https://agupubs.onlinelibrary.wiley.com/doi/10.1029/2023JC020627, Wiley Online Library on [18/06/2024]. See the Terms and Conditions (https://onlinelibrary.wiley.com/terms-and-conditions) on Wiley Online Library for rules of use; OA articles are governed by the applicable Creative Commons License

21699291, 2024, 4, Downloaded from https://agupubs.onlinelibrary.wiley.com/doi/10.1029/2023JC020627, Wiley Online Library on [18/06/2024]. See the Terms and Conditions (https://onlinelibrary.wiley.com/terms-and-conditions) on Wiley Online Library for rules of use; OA articles are governed by the applicable Creative Commons License

Reanalysis estimates of the wind speed were used to study the TC control on the ocean response. ERA5 Hourly reanalysis of 10-m wind components at 0.25° × 0.25° resolution was obtained from 2001 to 2022 (Hersbach, et al., 2018).

The upper ocean response was assessed using Argo float profile data before and after TC passage. Data from 2995 Argo floats between 2001/01/01–2023/07/01 and within 140°E—140°W and 0°S—60°S were retrieved (Argo, 2020). To ensure good data quality, delayed mode data flagged "Good," and "Probably Good" quality were selected.

2.2. Analysis

2.2.1. Argo-TC Matching

Argo float profiles with at least one pre-TC and one post-TC profile are selected. The pre-TC profile is between 15 and 3 days before the TC passes overhead, while the post-TC profile must be within 7 days of the TC passing and within twice the 34-knot wind radius (R_{34}) of the TC. Profiles were only selected if there is valid data between 0 and 500 m depth and profiles with a data gap larger than 20 m were discarded. Each Argo profile was linearly interpolated onto a uniform vertical grid with 2 m spacing. The profiles were divided into those on the left or right side of TC based on the direction of the TC movement. The distance from each post-TC profile to the TC was calculated as the minimum distance from the profile location to the line linking the two nearest TC tracking points, similar to the approach of Lin et al. (2017). At least one Argo profile pair with valid data was found for 136 TCs or Tropical Storms (intensity between 34 and 63 knots) and 1,296 profiles were collected within 7 days of a TC passing (Figure 1).

The temperature and salinity anomalies are calculated as the difference between the post-TC profile and the pre-TC profiles. Water density is calculated using the routines from the Gibbs-SeaWater (GSW) Oceanographic Toolbox (McDougall & Barker, 2011). The isothermal MLD of each profile is calculated using Patel (2023), with a 0.2°C temperature difference threshold from the surface.

2.2.2. Local Wind Power Dissipation

To consider both the influence of the TC intensity and its translation speed on ocean, we calculated the Local Wind Power Dissipation (PD_L). Bister and Emanuel (1998) assessed the total PD across the entire TC wind field, and Emanuel (2005) calculated the PDI by integrating the 1-min maximum sustained wind speed over the entire TC wind field. In this study, we refined the approach proposed by Emanuel (2005) to directly compute PD_L above the location of the profile. This is achieved using the ERA5 reanalysis winds, as only the area directly above the profile accurately reflects the local wind conditions experienced by the ocean at that specific location. PDI based on the TC V_{max} is not well correlated with the SSC recorded locally by Argo profiles (Figure S3 in Supporting Information S1). It's important to note that the PD calculated in this study includes wind power from sources other than TCs. Additional analysis shows that the difference between PD_L calculated between 3 days before and after TC passage (Figure S2 in Supporting Information S1) and PD_L calculated over 10 days, as in this study, is small. This suggests that the contribution of PD from sources other than TCs is limited.

PD_L was calculated over the time (typically 10 days) between consecutive Argo float profiles:

$$PD_L = \int_{t_0}^{t_1} \rho C_D V^3 dt \tag{1}$$

$$C_D = \begin{cases} 1.2, & V \le 11(m/s) \\ 0.49 + 0.065 \times V, & 11 \le V \le 28 \\ 2, & 28 \le V \le 41 \\ 1.9, & 41 \le V \le 50 \\ 1.5, & 50 \le V \end{cases} \tag{2}$$

21699291, 2024, 4, Downloaded from https://agupubs.onlinelibrary.wiley.com/doi/10.1029/2023JC020627, Wiley Online Library on [18/06/2024]. See the Terms and Conditions (https://onlinelibrary.wiley.com/terms-and-conditions) on Wiley Online Library for rules of use; OA articles are governed by the applicable Creative Commons License

where **t** is the time in seconds from the initial Argo profile, $\mathbf{t_0}$ to the post-TC profile, $\mathbf{t_1}$, **ρ** is sea surface air density, assumed to be 1 kg/m^3, $\mathbf{C_D}$ is the wind drag coefficient calculated using the corresponding hourly wind speed, and **V** is the hourly wind speed in m/s interpolated from the ERA5 wind speed gridded data to the location of the Argo profile. There are many different theories regarding $\mathbf{C_D}$ at high wind speed. Here we used the scheme tested by Zedler et al. (2009, Table 2A) based on Powell et al. (2003) and Large and Pond (1981) (Equation 2).

2.2.3. Cooling Inhibition Index

To describe the state of the initial upper ocean and its resistance to mixing, we used the Cooling Inhibition index (CI) developed by Vincent et al. (2012). CI is the cube root of the potential energy change that would be required to reduce the SST by 2°C. It is adopted as follows:

$$\Delta E_P = \int_{h_m}^{0} \left(\rho_f - \rho_i(z)\right) g z dz \tag{3}$$

$$\mathrm{CI} = \sqrt[3]{\Delta E_p} \tag{4}$$

where $\mathbf{h_m}$ is the mixing depth required to generate 2°C SSC. Since the minimum depth for Argo data is 2 m, we assumed the surface temperature and salinity to be the same as that at 2 m depth. Mean water temperature is calculated from the surface downward until the average temperature is 2°C below the SST and that depth defines $\mathbf{h_m}$. The calculation finds a new ML with uniform potential density ($\boldsymbol{\rho_f}$) from the surface to $\mathbf{h_m}$ that is the result of mixing the initial, observed potential density, $\boldsymbol{\rho_i(z)}$.

2.2.4. Background Variability

To determine if the observed changes in water properties after a TC passage are significant, we compare them with the local background variability. Regional background levels of temperature and salinity variability are calculated between consecutive profiles using all Argo floats from the South Pacific. The Argo profiles are divided by months and into 2° × 2° latitude/longitude grids by their location. Then the changes in temperature (ΔT), salinity (ΔS) and estimated isotherm displacement for each profile pair and the standard deviations for each grid cell are calculated.

The significance level of ΔT, ΔS and thermocline displacement at the time of the TCs is calculated by comparing each property to the standard deviation of the average background changes of the respective month and in the same 2° × 2° grid cell. For example, $\mathbf{\Delta T}$ is calculated from a profile pair before and after a TC and divided by $\boldsymbol{\sigma(\Delta T)}$, the background changes at the same depth in the same region, to find the significance level of the changes due to the TC. Average significance levels are shown on the relevant figures to indicate changes that are greater than one or two standard deviations from the expected background variability.

$$\mathrm{Significance}(ix,z) = \overline{\Delta T_{\mathrm{prof}}(z)/\sigma\Delta T_{\mathrm{background}}(z)} \tag{5}$$

Large-scale ocean motions, such as currents, are ignored. The Argo floats freely drift in the ocean, so horizontal gradients are difficult to estimate, and they may be significant in regions of strong currents such as the East Australian Current (Ridgway & Godfrey, 1997). Given most Argo floats drift 50 km or less between profiles, we assume that the difference in the ocean on these scales has minimal impact on the overall composite.

2.2.5. Upwelling

Upwelling was estimated by the isotherm displacement between profile pairs. We use linear interpolation to find the changes in depth between the pre-TC and post-TC temperatures through the water column. For example, 14°C may be at 300 m in the first profile and at 250 m after the TC passage. The difference in depth is the estimated upwelling, in this example, 50 m of upward vertical displacement. This method to estimate the upwelling displacement is only used at 50 m below the surface because upper ocean mixing prevents its application in the ML.

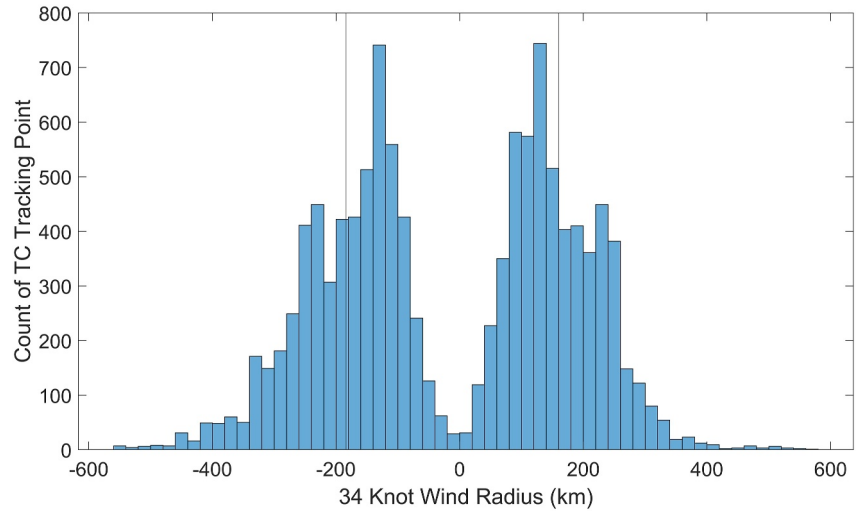

Figure 2. Distribution of the left and right side 34-knot wind radius, or R_{34}, of the South Pacific TCs between 2000 and 2023. Negative (positive) is on the left (right) side. The two vertical lines show the average R_{34} on the left and right sides.

2.3. The Normalized TC Cross-Track Segment

To account for the different radii of TCs and improve sampling, we scale the distance data by the R_{34} of the TC for that Argo location to create a canonical TC with a canonical ocean response. To do this, we combine the changes based on the relative distance from the TC center. Each Argo profile samples the ocean on one side of the TC and at one distance from the TC track. The distribution of R_{34} across the different TCs for all the Argo profile pairs is shown in Figure 2 and indicates considerable differences in the size of the TCs. The mean R_{34} on the left and right sides are 215 ± 129 km and 208 ± 122 km, respectively. The common approach of combining the changes from the profiles by absolute distances will smooth the signal because it will average different locations within the TC structure. Zhang, Lin, et al. (2019) also found that the size of TC cold wakes has a strong correlation with the 12 m/s (23 knots) wind radius of the TC. We maintain the position of the floats relative to the TC structure by averaging the profiles into a cross-track composite normalized by TC cross-track distance.

We normalize the distance of each Argo profile from the TC center by dividing the distance by the R_{34} of the TC quadrant in which the profile is located. The normalized distance is negative (positive) on the left (right) side. For example, if a profile is located 74 km to the left side of a TC, in the northeast quadrant which has an R_{34} of 200 km, then this profile has a relative distance of −0.37 R_{34}. Another profile 172 km to the right side of the same TC with the same R_{34} on that quadrant would have a relative distance of 0.86 R_{34}. We divide the normalized TC segment into 41 bins with 20 bins on each side of the TC extending to 2 R_{34}, each bin 0.1 R_{34} wide around a bin at 0 centered on the TC track. The Argo profiles are grouped into these bins. Bins with fewer than 5 Argo profiles are excluded to avoid small numbers of profiles influencing the result. For simplicity, the relative locations are henceforth written as **n** R_{34}, where **n** is the relative location from the center (0 R_{34}) to the R_{34}, and negative (positive) values are on the left (right) side of the track.

3. The Average Cross-Track Response

3.1. Example Argo Profile Pairs at Different Cross-Track Locations

Typical examples of observed Argo profiles before and after the passage of a TC are shown in Figure 3, focusing on the top 600 m Figure 3a (float 2902553, 2016 TC Victor, V_{max} 75 knots, 0 R_{34}) shows a response under the TC center. Here, the water temperature decreased monotonically through the water column above 800 m after the TC passed, consistent with upwelling, with a slightly deeper ML. Salinity increased within the ML, consistent with deeper, saltier water being mixed into the MLD as the TC passes. Below the ML, the depth of maximum salinity

21699291, 2024, 4, Downloaded from https://agupubs.onlinelibrary.wiley.com/doi/10.1029/2023JC020627, Wiley Online Library on [18/06/2024]. See the Terms and Conditions (https://onlinelibrary.wiley.com/terms-and-conditions) on Wiley Online Library for rules of use; OA articles are governed by the applicable Creative Commons License

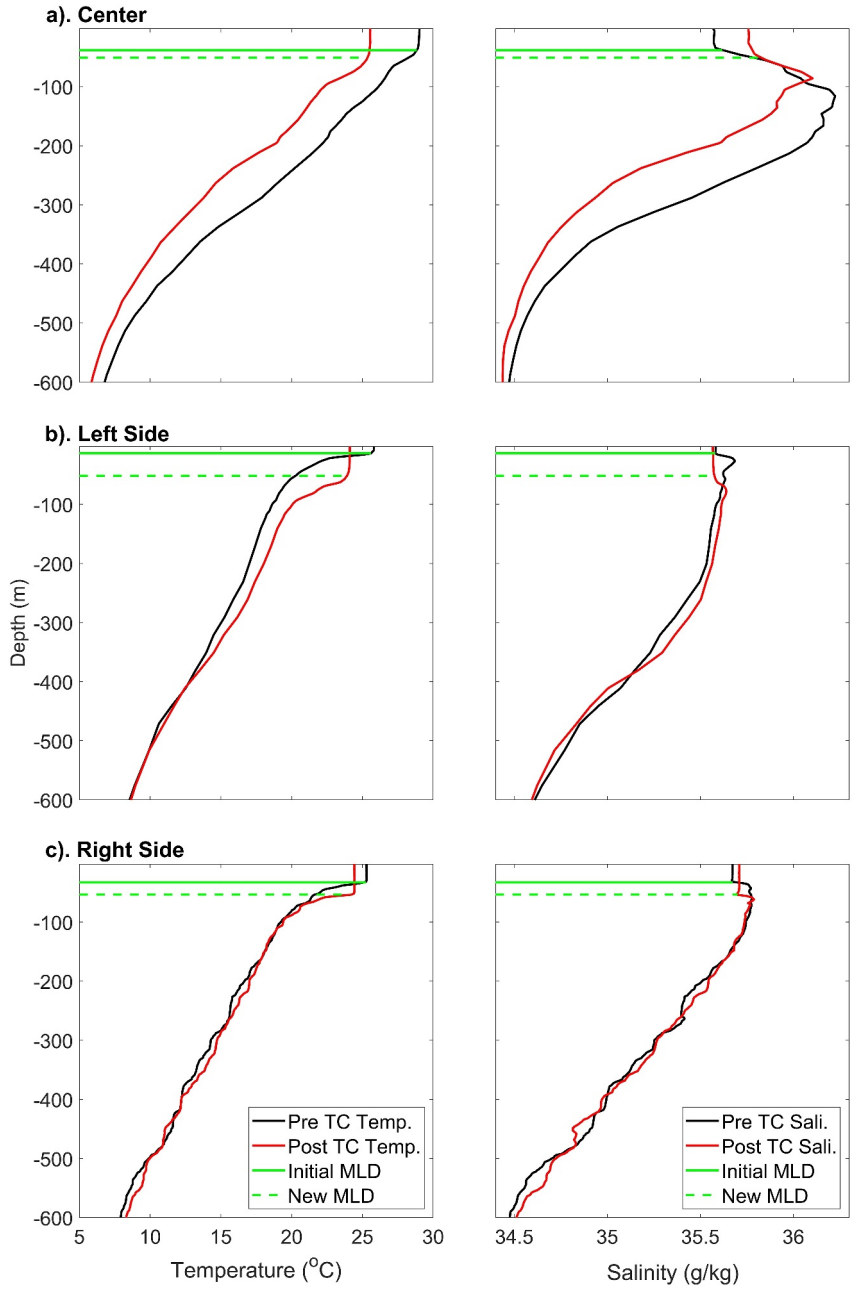

Figure 3. Examples of temperature (left) and salinity (right) profile pairs from the (a) center, (b) left and (c) right side of the TC track. The black lines show the initial profiles, the red line shows the post-TC profile, the green lines show the initial (solid) and post-TC (dashed) isothermal MLDs estimated from temperature profiles. Note that the Argo profiles have 10, 6, and 2 m depth sampling respectively.

rises from 116 to 86 m and the maximum salinity has reduced. Below the salinity maximum, salinity decreased monotonically to over 600 m. The observed temperature and salinity responses are consistent with upwelling, where the entire water column is uplifted, resulting in freshening below the salinity maximum and cooling down to 800 m.

Figure 3b (float 5901263, 2011 TC Zelia, V_{max} 65 knots, −0.7 R_{34}) measured a location on the left side of the TC track where the ML deepened considerably from 14 to 62 m. Water temperature in the later profile has warmed

21699291, 2024, 4, Downloaded from https://agupubs.onlinelibrary.wiley.com/doi/10.1029/2023JC020627, Wiley Online Library on [18/06/2024]. See the Terms and Conditions (https://onlinelibrary.wiley.com/terms-and-conditions) on Wiley Online Library for rules of use; OA articles are governed by the applicable Creative Commons License

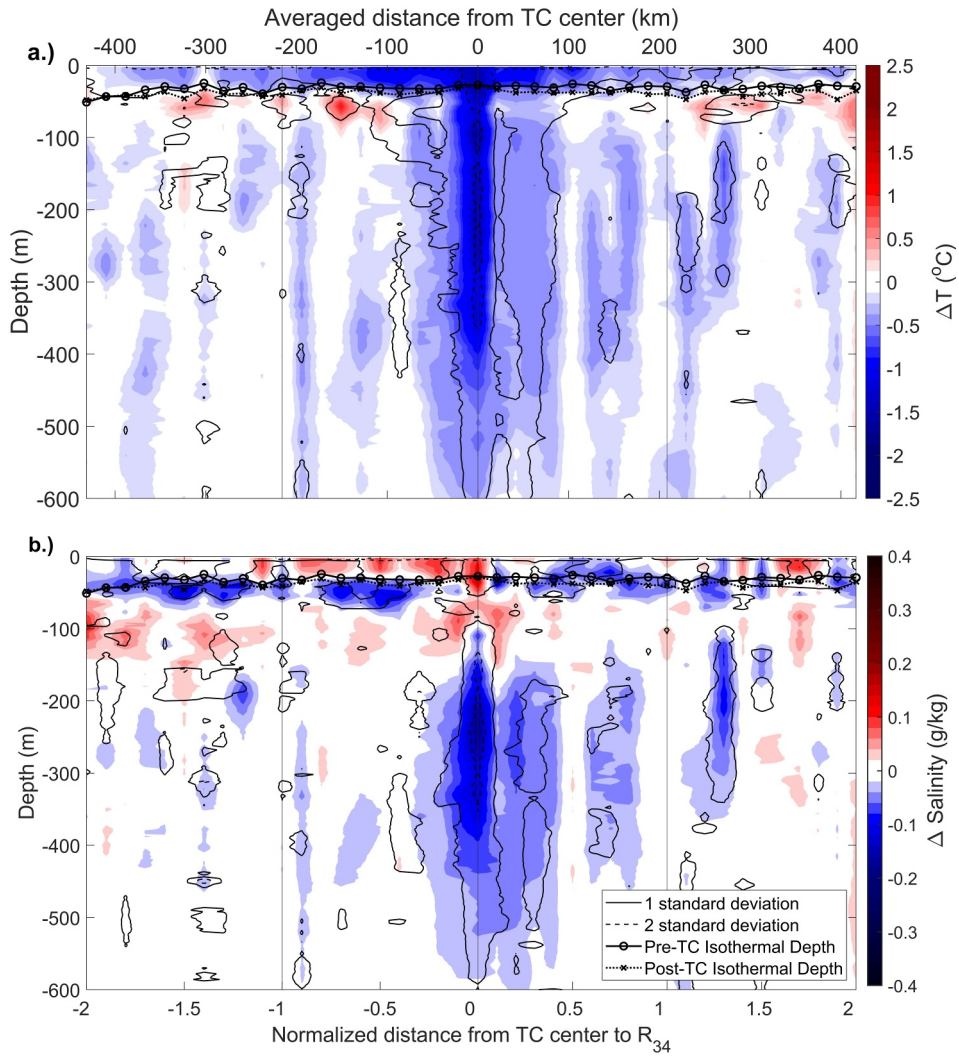

Figure 4. The average temperature (a) and salinity (b) changes within 7 days after the TC passage from a composite of 1,275 profile pairs. The lower *x*-axis shows the normalized distance from the TC center to the R_{34} on each side of the TC. For reference, the top *x*-axis shows the distance from the TC center for the average R_{34} from all the TCs used in the composite to give a sense of the distances. The solid (dashed) lines near the surface show the initial (post-TC) MLD. The thinner solid (dashed) contours show 1 (2) standard deviation from background levels.

monotonically in the thermocline down to 410 m compared to the initial profile. Salinity decreased throughout the new ML. The top of the halocline is displaced from 26 to 76 m in depth with a reduced maximum salinity. Between 76 and 400 m this depth, salinity is monotonically higher than the initial profile in the halocline. This response is consistent with downwelling, where the water column is displaced downward, pushing warmer, saltier water to greater depths, resulting in increased salinity and temperature below the new ML.

Figure 3c (float 5902431, 2019 TC Pola, V_{max} 60 knots, 0.5 R_{34}) shows a typical ocean response on the right side of a TC track. The ML has deepened from 32 to 52 m, resulting in cooling above the original ML and warming below. At 68 m below the surface, the water temperatures before and after the TC were very similar and that similarity continues to the bottom of the profiles at 2,000 m. The deepening of the ML has increased the salinity above 32 m and reduced the salinity in the ML below this depth. At 60 m depth, the salinities of the two profiles are very similar and they remain similar at deeper depths with minor fluctuations. In this profile pair, the temperature and salinity profiles below the new ML were very similar to the pre-TC profiles.

21699291, 2024, 4, Downloaded from https://agupubs.onlinelibrary.wiley.com/doi/10.1029/2023JC020627, Wiley Online Library on [18/06/2024]. See the Terms and Conditions (https://onlinelibrary.wiley.com/terms-and-conditions) on Wiley Online Library for rules of use; OA articles are governed by the applicable Creative Commons License

21699291, 2024, 4, Downloaded from https://agupubs.onlinelibrary.wiley.com/doi/10.1029/2023JC020627, Wiley Online Library on [18/06/2024]. See the Terms and Conditions (https://onlinelibrary.wiley.com/terms-and-conditions) on Wiley Online Library for rules of use; OA articles are governed by the applicable Creative Commons License

3.2. The Cross-Track Average Temperature Change

Figure 4 shows the average ΔT and ΔS within 7 days of the passage of a TC grouped by the normalized distance from the TC center. Note that all data between 0 and 7 days since the TC passing are merged in this study. There could be differences in the response measured between 1 and 7 days, however, with limited data in the region we cannot reliably resolve these differences. A version of this plot going down to 1,000 m is shown in Figure S1 in Supporting Information S1. Strong SSC is observed over the whole track with greater values on the left side of the TC as shown in Figure 3b. The greatest surface cooling was a decrease of over −0.6°C concentrated between −0.8 and 0.5 R_{34}. On the left side, the area between −0.5 and −0.8 R_{34} and below the ML between 36 and 88 m depth warmed over 0.3°C, with a maximum warming of 1°C at −0.7 R_{34} and 58 m depth. Warming on the right side of the TC was much smaller, no more than 0.22°C. Beyond R_{34} on both sides, the upper ML is cooled by less than 0.5°C. Below the initial ML, between ±1.5–2 R_{34}, several large warming patches extend from 30 to 100 m in depth, but only small parts of these are statistically significant. Under the TC center, strong cooling extended down to 600 m depth. Cooling over −1°C extended to 180 m depth, with a maximum cooling of −1.6°C. Cooling of −0.9°C and −0.6°C extended very deep: to 384 and 450 m, respectively.

ML deepening between 1.2 and 18 m, with an average of 7 ± 0.9 m, is observed across the cross-section to ±2 R_{34}, with no distinct left/right difference. MLD change becomes negligible at −1.8 R_{34} on the left side and 2.3 R_{34} on the right. The ML under the TC center on average shoals 1.2 m. This shoaling, coupled with the strong monotonic cooling at this location down to 600 m, suggest the shoaling MLD here is a result of strong upwelling under the TC center. Away from the TC center, cooling below the initial ML extended to a maximum depth of 44 m.

3.3. The Cross-Track Average Salinity Change

The average salinity changes in the upper ocean display a distinct leftward bias (Figure 4b). On the left side, surface salinity increased over 0.05 g/kg between −1 R_{34} and the TC center, peaking near the surface at 0.09 g/kg. Below the ML, between 30 and 74 m depth, general freshening over 0.05 g/kg is observed from −0.1 R_{34}, outward. On the right side, the surface salinity largely freshened. Under the TC center, a small patch of increased salinity, up to a magnitude of 0.12 g/kg, is observed down to 56 m depth. Increased salinities are also observed between 70 and 150 m at −0.2–0.1 R_{34}. The salinity increase at this depth suggests high salinity water has been displaced upward as seen in Figure 3a. Below 150 m under the TC center, a large area of reduced salinity is observed, extending down to 448 m depth, with a maximum salinity reduction of −0.19 g/kg at 240 m depth. This is consistent with uplifting of the whole water column because salinity decreases with depth below the mixed layer.

4. Upwelling Under the TC Center

Strong upwelling signals are observed under the TC center and slightly to the left, mainly between −0.1 R_{34} and 0 R_{34} (Figure 5) and at depths between 150 and 400 m. Under the TC center, a narrow, funnel-shaped region has significant upwelling with over 45 m of thermocline displacement at about 186 m depth. Upwelling over 20 m extends to about 1,000 m depth. This strong upwelling center is highly concentrated; the extended upwelling area beyond the TC center has only about 5–10 m of upward displacement. The average upwelling between −0.1 and 0 R_{34} and 100–400 m was 23.7 ± 3.5 m, which translates to about 2.4 m/day of upwelling averaged over the 10-day interval between Argo profiles.

Downwelling is mainly observed at ±0.5–2 R_{34}. The downwelling signal is much less concentrated than the upwelling signal, and the maximum downward displacement is only about 12 m, much weaker than the maximum upward displacement. Weak downward displacements of 5–7 m extend from 80 to 300 m at −0.7 and −1.5 R_{34} on the left side. This translates to about 0.5–0.7 m/day of downwelling averaged over the 10-day interval between Argo profiles. Downwelling between 2 and 5 meters extended from 60 to 180 m at −1.2 — −1.4 R_{34} on the right side. The downwelling signals are not statistically significant. This may mean that the downwelling is comparable to the level of the background displacement or that significant downwelling is less common than the upwelling signal. Some small regions of downwelling are observed on the outer edges of the TC between ±1.4–1.7 R_{34} on both sides of the track.

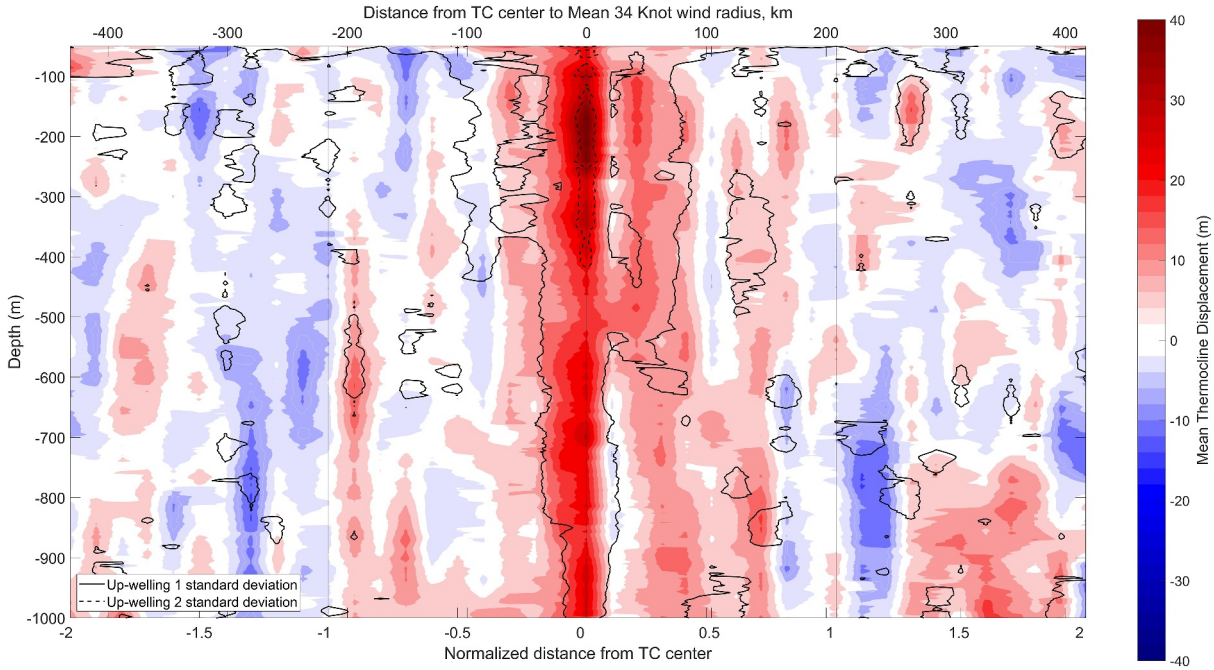

Figure 5. Average isotherm displacement within 7 days after the passage of a TC. Positive values are upward displacements of the isotherms. The solid (dashed) contours show 1 (2) standard deviation from background variations. Axes and significance levels are as in Figure.

5. The Atmospheric and Oceanic Controls: Local Wind Power Dissipation and Cooling Inhibition Index

5.1. Correlation of Local Wind Power Dissipation and Cooling Inhibition Index With the Upper Ocean Changes

To investigate the relationship between the TC and upper ocean controls on the temperature change in the ML, we adopted a method similar to that used by Vincent et al. (2012) to compare the effects of PD_L and CI on the ML temperature change within ± 1 R_{34}. Profiles with strong upwelling signals are removed by excluding post-TC profiles with average thermocline displacements over 22 m (1σ from the background level) between 100 and 400 m depth. The remaining profiles are binned into CI bins 2 units and PD_L bins 2×10^5 J wide. Note that here we used ocean observations and actual PD_L values while Vincent et al. (2012) used output from a simulation in their study and normalized the PD_L by an idealized tropical depression.

A trend of increasing SSC with higher PD_L and lower CI can be seen in Figure 6a, consistent with Figure 8a in Vincent et al. (2012). The bottom of the new ML (estimated from the new MLD in each post-TC profile, Figure 6b) tends to be warmer with higher PD_L and lower CI. This reflects stronger mixing with higher input of wind power and lower resistance from the pre-cyclone stratification, mixing more warm surface water to the bottom of the new ML. The same can also be observed with MLD change (Figure 6c), where stronger ML deepening is correlated with higher PD_L and lower CI. When the CI is high, some of the observations show the ML can become shallower. This response could be the result of ML shoaling with high CI hindering mixing, suggesting that the TC mixing cannot penetrate the initial ML at high CI.

5.2. The Temperature and Salinity Response as a Function of Wind Power Dissipation and Cooling Inhibition Index

To investigate specific controls of PD_L and CI on the upper ocean response, the Argo profiles are grouped into those with threshold of initial 30 CI and 1.5×10^6 J PD_L. Each group contains roughly half of the valid observations. The minimum number of profiles in each bin is reduced to 2 to include more data.

21699291, 2024, 4, Downloaded from https://agupubs.onlinelibrary.wiley.com/doi/10.1029/2023JC020627, Wiley Online Library on [18/06/2024]. See the Terms and Conditions (https://onlinelibrary.wiley.com/terms-and-conditions) on Wiley Online Library for rules of use; OA articles are governed by the applicable Creative Commons License

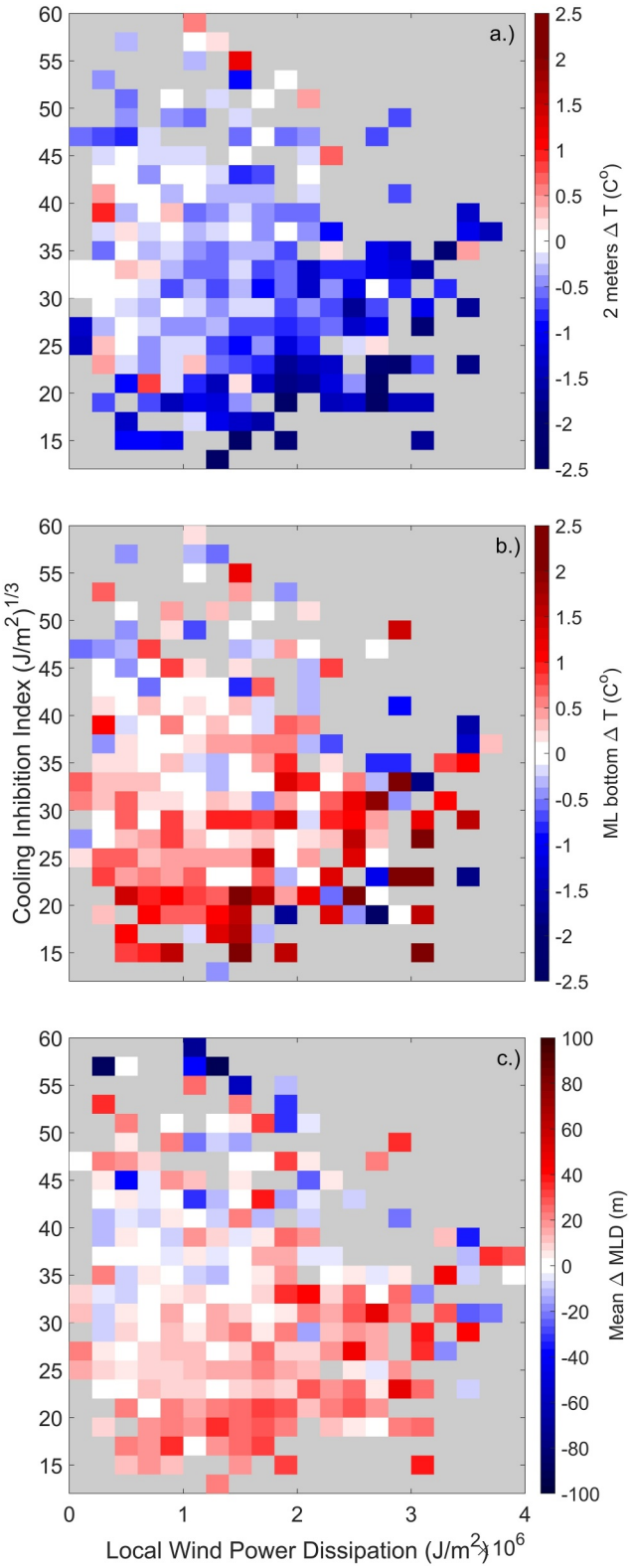

Figure 6. Relationship between Cooling Inhibition Index, overhead Local Wind Power Dissipation, and the average water temperature change (a) at the surface, (b) at the bottom of the post-TC mixed layer, and (c) with ΔMLD. Profiles with strong upwelling signals are removed.

In both low CI cases (Figures 7a and 7c), the average CI within R_{34} is 24, and the initial MLD is 22 ± 0.9 m. When CI and PD_L are low (Figure 7a), the surface SSC was relatively weak, reaching a maximum of −1.1°C at −0.2 R_{34}. Except for under the TC center, warming occurs at depths below the pre-TC ML across the track. Notably, the cold center was much weaker under the TC center (0 R_{34}) than the overall average (Figure 4a) and concentrated on the left side (0 and −0.1 R_{34}). Most temperature decreases were less than 0.5°C peaking at 1.26°C on the left side. The MLD within ±1 R_{34} increased 11 ± 1.2 m on average, larger than the average over all the observations (Figure 4a). Most of the salinification (Figure 8a) was concentrated in the top 30 m between −1.2 and 0 R_{34} on the left side. Some increases in salinity are also observed beyond 1.2 R_{34} on the right side. Freshening is observed below the salinification between −1.2 and 0 R_{34} on the left side and extending to the surface beyond −1.2 R_{34}. The surface was dominated by freshening on the right side between 0 and 1.2 R_{34}. The large freshening core seen in the average over all conditions (Figure 4b) was not observed.

With high PD_L (Figure 7c), the SSC is much stronger, and extended further from the TC center, with cooling over −2°C observed to R_{34} on both sides. Peak cooling of −2.1°C can be observed at ±0.1 R_{34} on both sides of the track. Below the initial ML, the subsurface warming is also much stronger, peaking at 2.3°C at 0.9 R_{34} on the right side and 2.1°C at −0.7 R_{34} on the left side. A large region of cooling stronger than the low PD_L case (Figure 7a) can be observed under the TC center. The average MLD deepening within ±1 R_{34} was 15.6 ± 2.8 m, much larger than the overall average of 7 ± 0.9 m (Figure 4a) and the low CI case (Figure 7a). The salinity changes for higher PD_L (Figure 8c) are patchier, but stronger and extended deeper than in the low PD_L case. The right side was dominated by weak freshening below the surface. Salinification under the TC center to 150 m depth and freshening to 500 m is observed, consistent with upwelling.

When CI is high (Figures 7b and 7d), the strong contrast between cooling at the surface and deeper warming (seen in Figures 7a and 7c) is not observed. The low PD_L case (Figure 7b) shows weak surface cooling of about 0.5°C while the cooling core under the TC center peaked at 2.3°C and only extended to about 450 m. The ΔMLD within ±1 R_{34} is 0 ± 2 m with shoaling of 19.1 m under the TC center. The salinity change was also weak (Figure 8b), while some weak surface salinification and subsurface freshening under the TC center were observed.

When PD_L was high (Figure 7d), many bins had no data, so the resulting image must be interpreted cautiously. Stronger SSC in the initial ML up to 2°C is observed on both sides of the track. Warming below the ML was hard to observe. Under the TC center, strong cooling over −1°C can be observed extending down to 500 m depth, with peak cooling of −2.8°C. In both cases, SSC is observed, and the peak cooling increases with PD_L. However, subsurface warming is minimal compared to cases when CI is low (Figures 7a and 7c). MLD within R_{34} deepened on average 5.9 ± 3.2 m, much weaker than for the low CI scenarios.

Upwelling was consistent in all four cases, with stronger but not statistically significant upwelling under stronger PD_L, while CI appears to have little impact on upwelling strength. The average thermocline displacements between 100 and 400 m and −0.1—0 R_{34}. In Figure 7 are: (a) low PD_L, low CI: 24 ± 5 m, (b) high PD_L, low CI: 28 ± 8 m, (c) low PD_L, high CI: 22 ± 7 m; (d) high PD_L, high CI: 31 ± 16 m, respectively.

21699291, 2024, 4, Downloaded from https://agupubs.onlinelibrary.wiley.com/doi/10.1029/2023JC020627, Wiley Online Library on [18/06/2024]. See the Terms and Conditions (https://onlinelibrary.wiley.com/terms-and-conditions) on Wiley Online Library for rules of use; OA articles are governed by the applicable Creative Commons License

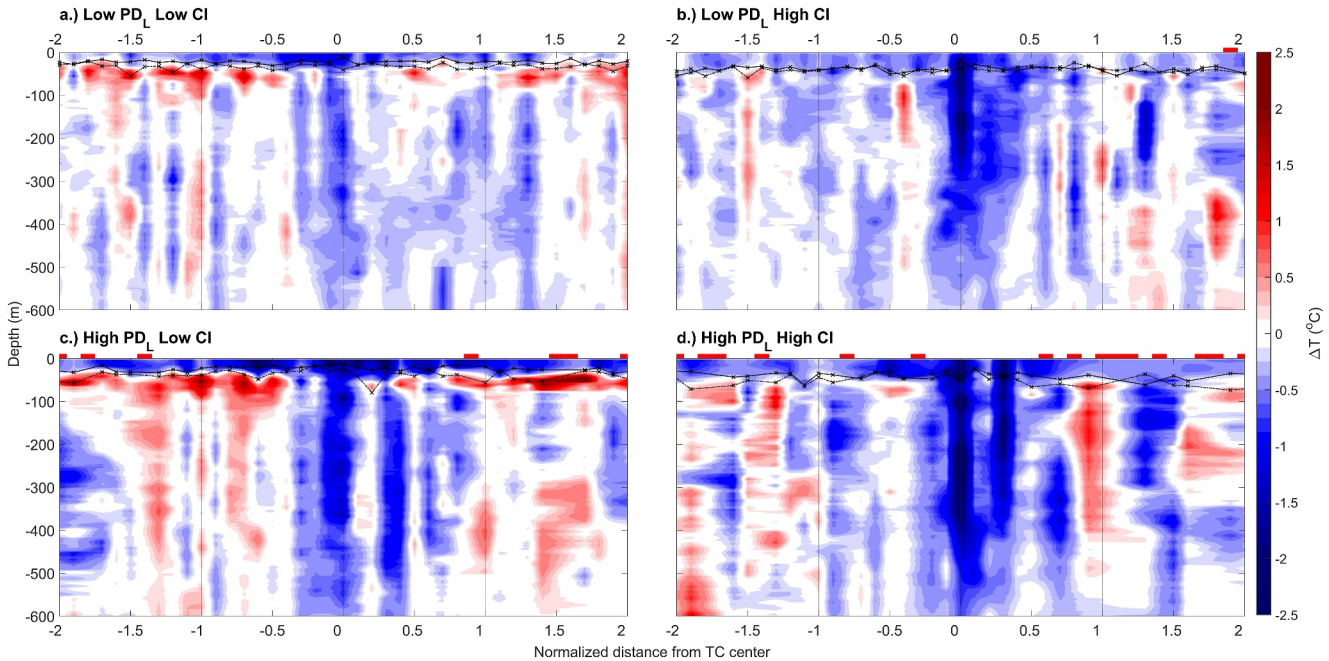

Figure 7. Average temperature changes from profiles with (a): low PD_L and low CI ($PD_L < 1.5 \times 10^6$ J and CI < 30; 291 profiles); (b): low PD_L and high CI (252 profiles), (c): high PD_L and low CI (119 profiles); (d): high PD_L and CI (92 profiles). Bins missing data are marked with red bars along the top axes. The solid (dotted) horizontal lines show the pre-TC (post-TC) MLD.

6. Discussion

6.1. Mixing-Induced Temperature and Salinity Responses

Argo float data show significant ocean changes due to the passage of TC in the South Pacific. Using a new method of normalizing the location of the profiles relative to the TC size shows a narrow region of very significant cooling

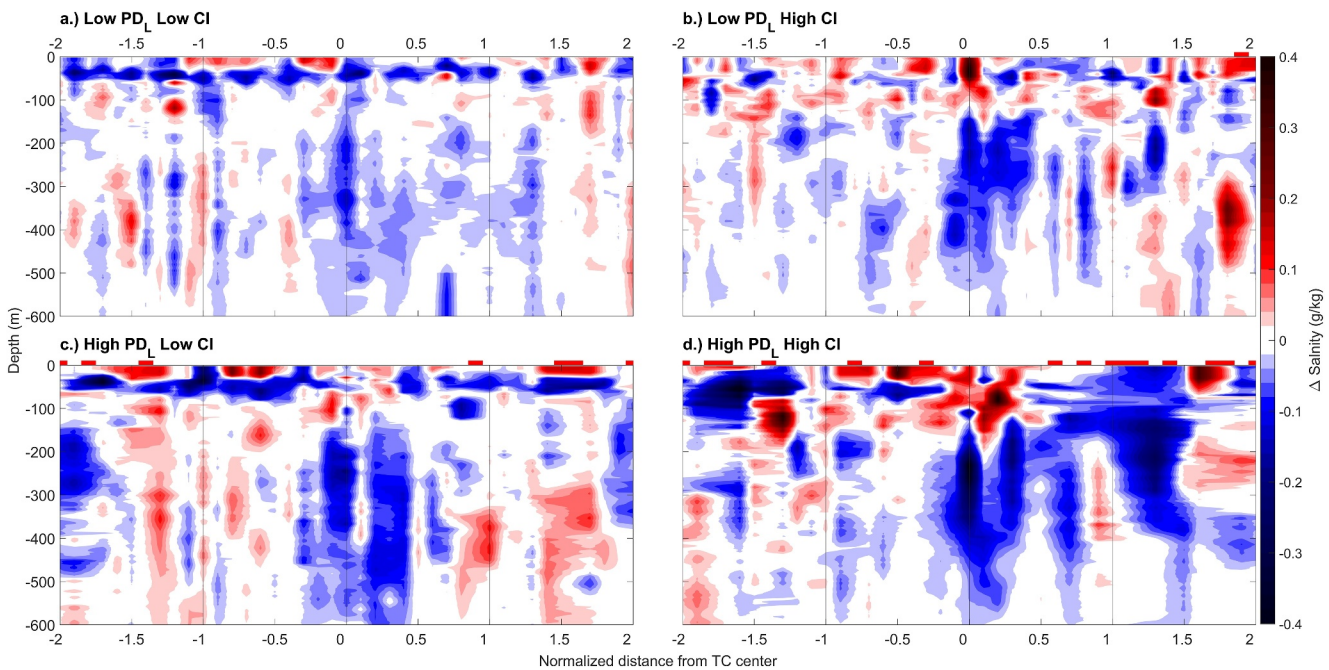

Figure 8. As for Figure 7, for average salinity change. MLDs are not shown.

21699291, 2024, 4, Downloaded from https://agupubs.onlinelibrary.wiley.com/doi/10.1029/2023JC020627, Wiley Online Library on [18/06/2024]. See the Terms and Conditions (https://onlinelibrary.wiley.com/terms-and-conditions) on Wiley Online Library for rules of use; OA articles are governed by the applicable Creative Commons License

21699291, 2024, 4, Downloaded from https://agupubs.onlinelibrary.wiley.com/doi/10.1029/2023JC020627, Wiley Online Library on [18/06/2024]. See the Terms and Conditions (https://onlinelibrary.wiley.com/terms-and-conditions) on Wiley Online Library for rules of use; OA articles are governed by the applicable Creative Commons License

under the TC center extending to over 500 m in depth. We observe cooling in the upper ML, with stronger cooling associated with the stronger side of the TC (the left side in the Southern hemisphere). The subsurface is characterized by strong cooling in the initial ML and warming below the initial ML within R_{34}, except for the region directly under the TC center where the ML shallows and cools. The upper ocean salinity structure on the left side is characterized by salinification in the initial ML and freshening below. This response is consistent with TC-induced mixing of surface warmer, fresher water in the initial ML with colder, saltier water below to form a new, deeper ML. Directly under the TC center, the response is consistent with upwelling.

The observed average ocean response in the South Pacific is similar to that previously observed from Argo floats in the Northwest Pacific (Cheng et al., 2015; Lin et al., 2017; Wang et al., 2016), although South Pacific TCs tend to be weaker which may result in less mixing. Despite the relative weakness of South Pacific TCs, the SSC found here is similar to that found in Northern Hemisphere studies. In our overall composite, we observed a peak surface cooling of −1.5°C under the TC center. Lin et al. (2017) observed an average SSC of about −1.2°C to the right of the track, 0.5° away from the center. Wang et al. (2016) observed an averaged maximum cooling of −1.4°C for TCs with a minimum V_{max} of 50 knots. Mei and Pasquero (2013) argued that TCs Cat.3 and over do not have increased SSC with wind speed. Supposing similar initial ocean conditions, it is possible that the reduced C_D under higher wind speed (Zedler et al., 2009) means the mechanical energy input into the upper ocean from the stronger Northern Hemisphere TCs is similar to that of the South Pacific TCs, resulting in similar SSC in both hemispheres.

The subsurface structure of the temperature and salinity changes we observed has similarities to the structures previously observed from Argo floats and found in simulations, but also some differences. In previous observations, for example, Zhang et al. (2018), and Lin et al. (2017), the strongest mixing often lies on the stronger side of the TC. This pattern is reflected in the temperature response (Figure 4a) as significant but weaker cooling extending to the weaker side (right side), but the width of the cold wake from the TC center here is smaller. The weaker side cold wake is also wider and stronger than the modeling results of Zhang et al. (2018). Surface salinification in this study (Figure 4b) is almost solely on the stronger side, with the weaker side dominated by freshening while in Lin et al. (2017), the stronger side is also dominated by salinification, but salinification also extends slightly to the weaker side. Another notable feature is the lack of downwelling-only region on the outskirts of the TC in Figures 4a and 5 compared to Northern Hemisphere observations like Zhang (2023). A likely reason is that the TC-induced downwelling is relatively weak owing to the general lower intensity of South Pacific TCs. The resulting downwelling at the outskirts of the TC is thus likely too weak to be distinguished from the background signals.

The averaged surface ΔS structure (Figure 4b) shows salinification on the stronger side and freshening on the weaker side of the TC's track. This pattern differs partially from Reul et al. (2021)'s analysis based on satellite data. Reul et al. (2021) found that Tropical Storms below Cat. 1 cause strong freshening on the weaker side of the track and weak salinification on the stronger side. The freshening on the weaker side (salinification on the stronger side) weakens (strengthens) with stronger TCs. Above Cat. 2, the TCs cause salinification across both sides of the track, strongest on the stronger side of the track. The surface salinity response observed in this study and in Lin et al. (2017) are both similar to Reul et al. (2021)'s weak TC cases.

The high structural resolution provided by this study provides evidence of the benefit of scaling the upper ocean response by the radius of the TC. This result also corroborates the observation of Zhang, Lin, et al. (2019) that the size of the TC surface cold wake is linked to the 12 m/s (23 knot) wind radius of the TC. Future studies using Argo floats would benefit from scaling the relative location of the profile with the TC radius.

6.2. The Cross-Track Water Displacement Patterns

Warming between ±1–2 R_{34} extends to 400 m, and a strong and concentrated cooling core extends to over 500 m depth under the TC center. Salinity under the TC center is characterized by salinification between 50 and 150 m and freshening below, which is consistent with the water in the thermocline being uplifted (see Figure 3b). The temperature changes suggest upwelling of over 30 m in the 200–300 m depth range under the TC's center and downwelling of up to 25 m at ±1.5–2 R_{34} through the same depths (Figure 5). These observations are consistent with a complete cross-track circulation cell. A notably weak ML deepening can be observed under the TC center (Figure 4) despite strong cooling, which likely results from the strong upwelling under the TC center bringing stratified water upward that counteracts the mixing-induced ML deepening.

21699291, 2024, 4, Downloaded from https://agupubs.onlinelibrary.wiley.com/doi/10.1029/2023JC020627, Wiley Online Library on [18/06/2024]. See the Terms and Conditions (https://onlinelibrary.wiley.com/terms-and-conditions) on Wiley Online Library for rules of use; OA articles are governed by the applicable Creative Commons License

The strong and deep cooling core being biased toward the stronger side of the TC as found in this study is consistent with observations in the Northern Hemisphere (Cheng et al., 2015; Lin et al., 2017; Zhang et al., 2018) and modeling results (Jullien et al., 2012). Lin et al. (2017) estimated an average displacement of the 14°C isotherm of 18.2 m, which is smaller than the 27.9 m displacement in this study. However, Lin et al. (2017) only captured a cooling core with the −0.4°C ΔT contour extending to above 400 m and about 100 km wide, while their −1°C ΔT contour is limited to above 150 m and wider. Cheng et al. (2015) captured a cooling core of −0.2°C ΔT extending to 200 m depth, and their −1°C ΔT contour is limited to the top 50 m. The pattern of stronger upwelling on the stronger side of the TC is consistent with modeling results (Zhang et al., 2018) and Lin et al. (2017)'s study based on the Northwest Pacific Argo observations and indicates that the strength of the upwelling is linked to the strength of the TC wind above. Lin et al. (2017) also observed that upwelling suppressed the subsurface warming signal below the TC track. In this study, this effect can be observed as an area of weaker cooling between two patches of strong cooling over −1.2°C between 50 and 100 m (Figure 4a). This is likely where the mixing-induced warming at the base of the new ML is suppressed by colder water from upwelling. Additionally, a positive salinity anomaly below the ML is also observed. This positive salinity anomaly between 70 and 150 m below the TC center is comparable to Lin et al. (2017)'s observations.

This study provides finer resolution of the upwelling core under the TC's center than previous studies using Argo floats, benefiting from finer bins, more data, and the relative distance approach. In this study, the −1°C ΔT contour extends to 380 m in depth and is much more concentrated below the TC center than in previous studies: the strongest part of the upwelling core is confined within bin 0 under the TC, roughly only 20 km wide. Cooling over −0.7°C extends to 416 m, with a peak cooling of −1.3°C at 118 m. Cooling over −0.5°C extends further to 600 m depth and extends into −0.1 R_{34} on the left to 382 m depth. This upwelling core is stronger and much narrower than that captured by Lin et al. (2017) and Cheng et al. (2015), although the extents of their −0.4°C and −0.2°C cooling contours are similar to this study. Their observations also show the upwelling core biased toward the weaker side of the TC, while in this study, the weaker contour of the upwelling core (−0.2/−0.4°C) is leaning to the weaker side, and the stronger cooling contour of −0.5°C and above is biased to the stronger side. More detailed observations of the upper ocean response to TCs will provide deeper insights into predicting the climate impacts of TC-ocean interaction and forecasting the strength of future TCs.

6.3. Linking Wind Power Dissipation and Cooling Inhibition Index to the Upper Ocean Response

A strong positive correlation is found between PD_L and surface cooling, subsurface warming in the top 150 m and deepening of the ML (Figure 6), indicating a strong correlation of PD_L with mixing. The warming trend at the bottom of the new ML is consistent with the theory proposed by Vincent et al. (2012). An inverse relationship is also found between CI and mixing.

Low CI cases represent situations when the upper ocean has lower resistance to mixing, either because the initial ML is shallow, the stratification at the base of the ML is weak, or both, with the result being enhanced vertical mixing. Here, TCs with the same wind speed and translation speed can produce more SSC and subsurface warming. Higher PD_L mainly increases the strength of upper ocean mixing and upwelling under the TC center, consistent with Vincent et al. (2012)'s modeling result. Previous observations show that higher wind speed, slower translation speed, shallower ML and weaker stratification create a strong SSC (Mei et al., 2015). The result here shows PD_L and CI efficiently describe the upper ocean response by combining all the parameters used in previous studies.

High CI (>30) cases are where the ocean's resistance is strong enough to limit the cooling from the wind-driven mixing due to the TC. A high CI means either the initial ML is deep, the initial stratification at the base of the ML is strong, or both, requiring more TC mixing to achieve the same SSC. In cases with high CI (Figures 7b and 7d), SSC is much weaker and there is little to no warming below the ML. This means the TC in these two scenarios forces very small changes below the ML, so less surface (subsurface) warm (cold) water is delivered to the thermocline (surface), and the cooling in the initial ML is likely more dominated by air-sea heat exchange. This is also reflected in the small average ML deepening of 1 and 5 m, respectively. The higher PD_L scenario is consistent with more energy from the TC wind counteracting the ocean stratification and creating slightly more cooling in the ML, subsurface warming, and ML deepening. It appears that in the South Pacific, when CI > 30, TCs would not have sufficient energy to penetrate the thermocline.

21699291, 2024, 4, Downloaded from https://agupubs.onlinelibrary.wiley.com/doi/10.1029/2023JC020627, Wiley Online Library on [18/06/2024]. See the Terms and Conditions (https://onlinelibrary.wiley.com/terms-and-conditions) on Wiley Online Library for rules of use; OA articles are governed by the applicable Creative Commons License

When CI < 30, there is a distinctive pattern of SSC and lower ML warming (Figures 7a and 7c). When CI > 30, the response is a weaker, deeper layer of upper ML cooling, with nearly no warming below in both high and low PD_L scenarios (Figures 7b and 7d). The upwelling core below the TC's center is present in all CI cases. This study found that higher PD_L could result in stronger upwelling under the TC's center, but the limited data are insufficient to eliminate outliers or form a strong relationship. The relationship between PD_L and upwelling is well described theoretically and is consistent with our observations: stronger PD_L induces stronger surface currents and displaces more water away from the TC center area (Hsu & Ho, 2019; Zhang et al., 2016).

The use of PD_L and CI in this study enables a more compact comparison of the ocean response with both the TC forcing and the pre-TC ocean conditions. Previous studies have considered TC wind speed and translation speed separately (Cheng et al., 2015; Lin et al., 2017; Mei et al., 2015), which divides the observations and reduces the data available, whereas Emanuel (1999a)'s PD enables a single parameter to account for these two factors. The same argument applies to Vincent et al. (2012)'s CI index, which combines the initial MLD and the strength of the stratification below the initial ML. WP and CI are the key controls on the ocean responses, but not the only ones. Other factors, like TC-induced precipitation, and consecutive TC passage, may also have impacts on the ocean response (Balaguru et al., 2022; Baranowski et al., 2014; Huang et al., 2009) and investigating these may further improve our understanding of the upper ocean response.

7. Conclusion

We average Argo float data near all available South Pacific TCs to form cross-track composites of the ocean response using a new method that scales the distance of the float by R_{34} to create a more dynamically consistent average. The composite results show the response can be characterized using the parameters PD_L and CI. We find that TCs create strong and deep-reaching upwelling under their center and there are robust relationships between observed mixed layer changes and the PD_L and CI parameters. Future studies could further examine the feasibility of using PD_L and CI as predictions of ocean response and investigate the upwelling effect induced by TCs in more detail, including its impact on phytoplankton. With better understanding from the observational record, future TC strength and the ocean response can be better predicted.

Data Availability Statement

All data used in this study are publicly available in the following sources. Observational data were provided by the Argo (2020) program (https://argo.ucsd.edu, https://www.ocean-ops.org). The Argo Program is part of the Global Ocean Observing System. Past TC track records were provided by the International Best Track Archive for Climate Stewardship (IBTrACS) Project (Knapp et al., 2018). The ERA5 surface u/v wind data in the ERA5 hourly data on single levels from 1959 to present data set (Hersbach, et al., 2018) were downloaded from the Copernicus Climate Change Service (C3S) Climate Data Store. Patel (2023) provided the Isothermal Layer Depth calculation codes. All data are processed using MATLAB Mathworks (2022).

Acknowledgments
Support for all authors was provided by the Deep South National Science Challenge. Philip Sutton had additional support from the NZ Ministry for Business, Innovation and Employment (MBIE) NIWA Strategic Investment Funding OCOC2404. Open access publishing facilitated by The University of Auckland, as part of the Wiley - The University of Auckland agreement via the Council of Australian University Librarians.

References

Argo. (2020). Argo float data and metadata from global data assembly center (Argo GDAC)—Snapshot of Argo GDAC of August 2020 [Dataset]. *SEANOE*. https://doi.org/10.17882/42182#76230

Balaguru, K., Foltz, G. R., Leung, L. R., & Emanuel, K. A. (2016). Global warming-induced upper-ocean freshening and the intensification of super typhoons. *Nature Communications*, *7*(1), 13670. https://doi.org/10.1038/ncomms13670

Balaguru, K., Foltz, G. R., Leung, L. R., & Hagos, S. M. (2022). Impact of rainfall on tropical cyclone-induced sea surface cooling. *Geophysical Research Letters*, *49*(10). https://doi.org/10.1029/2022GL098187

Balaguru, K., Taraphdar, S., Leung, L. R., Foltz, G. R., & Knaff, J. A. (2014). Cyclone-cyclone interactions through the ocean pathway. *Geophysical Research Letters*, *41*(19), 6855–6862. https://doi.org/10.1002/2014GL061489

Baranowski, D. B., Flatau, P. J., Chen, S., & Black, P. G. (2014). Upper ocean response to the passage of two sequential typhoons. *Ocean Science*, *10*(3), 559–570. https://doi.org/10.5194/os-10-559-2014

Bister, M., & Emanuel, K. A. (1998). Dissipative heating and hurricane intensity: Tropical cyclones. *Meteorology and Atmospheric Physics*, *65*(3–4), 233–240. https://doi.org/10.1007/bf01030791

Black, W. J., & Dickey, T. D. (2008). Observations and analyses of upper ocean responses to tropical storms and hurricanes in the vicinity of Bermuda. *Journal of Geophysical Research*, *113*(C8), C08009. https://doi.org/10.1029/2007JC004358

Bond, N. A., Cronin, M. F., Sabine, C., Kawai, Y., Ichikawa, H., Freitag, P., & Ronnholm, K. (2011). Upper ocean response to Typhoon Choi-Wan as measured by the Kuroshio extension observatory mooring. *Journal of Geophysical Research*, *116*(C2), C02031. https://doi.org/10.1029/2010JC006548

Cheng, L., Zhu, J., & Sriver, R. L. (2015). Global representation of tropical cyclone-induced short-term ocean thermal changes using Argo data. *Ocean Science*, *11*(5), 719–741. https://doi.org/10.5194/os-11-719-2015

Cione, J. J., & Uhlhorn, E. W. (2003). Sea surface temperature variability in hurricanes: Implications with respect to intensity change. *Monthly Weather Review*, *131*(8), 1783–1796. https://doi.org/10.1175//2562.1

Domingues, R., Goni, G., Bringas, F., Lee, S.-K., Kim, H.-S., Halliwell, G., et al. (2015). Upper ocean response to Hurricane Gonzalo (2014): Salinity effects revealed by targeted and sustained underwater glider observations. *Geophysical Research Letters*, *42*(17), 7131–7138. https://doi.org/10.1002/2015GL065378

Emanuel, K. (2002). A simple model of multiple climate regimes. *Journal of Geophysical Research*, *107*(D9), ACL4-1–ACL4-10. https://doi.org/10.1029/2001JD001002

Emanuel, K. (2003). Tropical cyclones. *Annual Review of Earth and Planetary Sciences*, *31*(1), 75–104. https://doi.org/10.1146/annurev.earth.31.100901.141259

Emanuel, K. (2005). Increasing destructiveness of tropical cyclones over the past 30 years. *Nature*, *436*(7051), 686–688. https://doi.org/10.1038/nature03906

Emanuel, K., Sundararajan, R., & Williams, J. (2008). Hurricanes and global warming: Results from downscaling IPCC AR4 simulations. *Bulletin of the American Meteorological Society*, *89*(3), 347–367. https://doi.org/10.1175/BAMS-89-3-347

Emanuel, K. A. (1986). An air-sea interaction theory for tropical cyclones. Part I: Steady-state maintenance. *Journal of the Atmospheric Sciences*, *43*(6), 585–605. https://doi.org/10.1175/1520-0469(1986)0432.0.CO;2

Emanuel, K. A. (1987). The dependence of hurricane intensity on climate. *Nature*, *326*(6112), 483–485. https://doi.org/10.1038/326483a0

Emanuel, K. A. (1988). The maximum intensity of hurricanes. *Journal of the Atmospheric Sciences*, *45*(7), 1143–1155. https://doi.org/10.1175/1520-0469(1988)0452.0.CO;2

Emanuel, K. A. (1991). The theory of hurricanes. *Annual Review of Fluid Mechanics*, *23*(1), 179–196. https://doi.org/10.1146/annurev.fl.23.010191.001143

Emanuel, K. A. (1999a). The power of a hurricane: An example of reckless driving on the information superhighway. *Weather*, *54*(4), 107–108. https://doi.org/10.1002/j.1477-8696.1999.tb06435.x

Emanuel, K. A. (1999b). Thermodynamic control of hurricane intensity. *Nature*, *401*(6754), 665–669. https://doi.org/10.1038/44326

Fisher, E. L. (1958). Hurricanes and the sea-surface temperature field. *Journal of Meteorology*, *15*(3), 328–333. https://doi.org/10.1175/1520-0469(1958)0152.0.CO;2

Girishkumar, M. S., Suprit, K., Chiranjivi, J., Udaya Bhaskar, T. V. S., Ravichandran, M., Shesu, R. V., & Pattabhi Rama Rao, E. (2014). Observed oceanic response to tropical cyclone Jal from a moored buoy in the south-western Bay of Bengal. *Ocean Dynamics*, *64*(3), 325–335. https://doi.org/10.1007/s10236-014-0689-6

Glenn, S. M., Miles, T. N., Seroka, G. N., Xu, Y., Forney, R. K., Yu, F., et al. (2016). Stratified coastal ocean interactions with tropical cyclones. *Nature Communications*, *7*(1), 10887. https://doi.org/10.1038/ncomms10887

Guan, S., Zhao, W., Sun, L., Zhou, C., Liu, Z., Hong, X., et al. (2021). Tropical cyclone-induced sea surface cooling over the Yellow Sea and Bohai Sea in the 2019 Pacific typhoon season. *Journal of Marine Systems*, *217*, 103509. https://doi.org/10.1016/j.jmarsys.2021.103509

Han, C. (2023). *Tropical cyclone induced upper ocean response in the South Pacific observed by Argo floats*. ResearchSpace@Auckland.

Hart, R. E., Maue, R. N., & Watson, M. C. (2007). Estimating local memory of tropical cyclones through MPI anomaly evolution. *Monthly Weather Review*, *135*(12), 3990–4005. https://doi.org/10.1175/2007MWR2038.1

Held, I. M., & Zhao, M. (2011). The response of tropical cyclone statistics to an increase in CO_2 with fixed sea surface temperatures. *Journal of Climate*, *24*(20), 5353–5364. https://doi.org/10.1175/JCLI-D-11-00050.1

Hersbach, H., Bell, B., Berrisford, P., Biavati, G., Horányi, A., Muñoz Sabater, J., et al. (2018). ERA5 hourly data on single levels from 1959 to present [Dataset]. *Copernicus Climate Change Service (C3S) Climate Data Store (CDS)*. https://doi.org/10.24381/cds.adbb2d47

Hsu, P.-C., & Ho, C.-R. (2019). Typhoon-induced ocean subsurface variations from glider data in the Kuroshio region adjacent to Taiwan. *Journal of Oceanography*, *75*(1), 1–21. https://doi.org/10.1007/s10872-018-0480-2

Huang, P., Lin, I.-I., Chou, C., & Huang, R.-H. (2015). Change in ocean subsurface environment to suppress tropical cyclone intensification under global warming. *Nature Communications*, *6*(1), 7188. https://doi.org/10.1038/ncomms8188

Huang, P., Sanford, T. B., & Imberger, J. (2009). Heat and turbulent kinetic energy budgets for surface layer cooling induced by the passage of Hurricane Frances (2004). *Journal of Geophysical Research*, *114*(C12). https://doi.org/10.1029/2009JC005603

Huang, R. X., Huang, C. J., & Wang, W. (2007). Dynamical roles of mixed layer in regulating the meridional mass/heat fluxes. *Journal of Geophysical Research*, *112*(C5), C05036–n/a. https://doi.org/10.1029/2006JC004046

Huber, M., & Sriver, R. L. (2007). Observational evidence for an ocean heat pump induced by tropical cyclones. *Nature*, *447*(7144), 577–580. https://doi.org/10.1038/nature05785

Jacob, S. D., & Koblinsky, C. J. (2007). Effects of precipitation on the upper-ocean response to a hurricane. *Monthly Weather Review*, *135*(6), 2207–2225. https://doi.org/10.1175/MWR3366.1

Jaimes, B., & Shay, L. K. (2009). Mixed layer cooling in mesoscale oceanic eddies during Hurricanes Katrina and Rita. *Monthly Weather Review*, *137*(12), 4188–4207. https://doi.org/10.1175/2009MWR2849.1

Jullien, S., Menkes, C. E., Marchesiello, P., Jourdain, N. C., Lengaigne, M., Koch-larrouy, A., et al. (2012). Impact of tropical cyclones on the heat budget of the South Pacific Ocean. *Journal of Physical Oceanography*, *42*(11), 1882–1906. https://doi.org/10.1175/JPO-D-11-0133.1

Knapp, K. R., Diamond, H. J., Kossin, J. P., Kruk, M. C., & Schreck, C. J., III. (2018). International best track archive for climate stewardship (IBTrACS) Project, version 4 [Dataset] [2022.2.1]. *NOAA National Centers for Environmental Information*. https://doi.org/10.25921/82ty-9e16

Kobashi, F., Doi, H., & Iwasaka, N. (2019). Sea surface cooling induced by extratropical cyclones in the subtropical North Pacific: Mechanism and interannual variability. *Journal of Geophysical Research: Oceans*, *124*(3), 2179–2195. https://doi.org/10.1029/2018JC014632

Korty, R. L., Emanuel, K. A., & Scott, J. R. (2008). Tropical cyclone–induced upper-ocean mixing and climate: Application to equable climates. *Journal of Climate*, *21*(4), 638–654. https://doi.org/10.1175/2007JCLI1659.1

Kossin, J. P., Knapp, K. R., Olander, T. L., & Velden, C. S. (2020). Global increase in major tropical cyclone exceedance probability over the past four decades. *Proceedings of the National Academy of Sciences of the United States of America*, *117*(22), 11975–11980. https://doi.org/10.1073/pnas.1920849117

Large, W. G., & Pond, S. (1981). Open ocean momentum flux measurements in moderate to strong winds. *Journal of Physical Oceanography*, *11*(3), 324–336. https://doi.org/10.1175/1520-0485(1981)011<0324:OOMFMI>2.0.CO;2

Lim, H. S., Miles, T. N., Glenn, S., Kim, D., Kim, M., Shim, J.-S., et al. (2020). Rapid ocean destratification by Typhoon Soulik over the highly stratified waters of west Jeju Island, Korea. *Journal of Coastal Research*, *95*(sp1), 1480–1484. https://doi.org/10.2112/SI95-285.1

Lin, I.-I., Chen, C.-H., Pun, I.-F., Liu, W. T., & Wu, C.-C. (2009). Warm ocean anomaly, air sea fluxes, and the rapid intensification of tropical cyclone Nargis (2008): Warm ocean anomaly and cyclone Nargis. *Geophysical Research Letters*, *36*(3). https://doi.org/10.1029/2008GL035815

21699291, 2024, 4, Downloaded from https://agupubs.onlinelibrary.wiley.com/doi/10.1029/2023JC020627, Wiley Online Library on [18/06/2024]. See the Terms and Conditions (https://onlinelibrary.wiley.com/terms-and-conditions) on Wiley Online Library for rules of use; OA articles are governed by the applicable Creative Commons License

Lin, I.-I., Pun, I.-F., & Wu, C.-C. (2009). Upper-ocean thermal structure and the western north pacific category 5 typhoons. Part II: Dependence on translation speed. *Monthly Weather Review*, *137*(11), 3744–3757. https://doi.org/10.1175/2009MWR2713.1

Lin, I.-I., Wu, C.-C., Emanuel, K. A., Lee, I.-H., Wu, C.-R., & Pun, I.-F. (2005). The interaction of Supertyphoon Maemi (2003) with a warm ocean eddy. *Monthly Weather Review*, *133*(9), 2635–2649. https://doi.org/10.1175/MWR3005.1

Lin, I.-I., Wu, C.-C., Pun, I.-F., & Ko, D.-S. (2008). Upper-ocean thermal structure and the Western North Pacific category 5 typhoons. Part I: Ocean features and the category 5 typhoons' intensification. *Monthly Weather Review*, *136*(9), 3288–3306. https://doi.org/10.1175/2008MWR2277.1

Lin, S., Zhang, W.-Z., Shang, S.-P., & Hong, H.-S. (2017). Ocean response to typhoons in the western North Pacific: Composite results from Argo data. Deep-sea research. Part I. *Oceanographic Research Papers*, *123*, 62–74. https://doi.org/10.1016/j.dsr.2017.03.007

Liu, L. L., Wang, W., & Huang, R. X. (2008). The mechanical energy input to the ocean induced by tropical cyclones. *Journal of Physical Oceanography*, *38*(6), 1253–1266. https://doi.org/10.1175/2007JPO3786.1

Liu, Z., Xu, J., Sun, C., & Wu, X. (2014). An upper ocean response to Typhoon Bolaven analyzed with Argo profiling floats. *Acta Oceanologica Sinica*, *33*(11), 90–101. https://doi.org/10.1007/s13131-014-0558-7

Liu, Z., Xu, J., Zhu, B., Sun, C., & Zhang, L. (2007). The upper ocean response to tropical cyclones in the northwestern Pacific analyzed with Argo data. *Chinese Journal of Oceanology and Limnology*, *25*(2), 123–131. https://doi.org/10.1007/s00343-007-0123-8

Lloyd, I. D., & Vecchi, G. A. (2011). Observational evidence for oceanic controls on hurricane intensity. *Journal of Climate*, *24*(4), 1138–1153. https://doi.org/10.1175/2010JCLI3763.1

Mainelli, M. M., DeMaria, M., Shay, L. K., & Goni, G. (2008). Application of oceanic heat content estimation to operational forecasting of recent Atlantic category 5 hurricanes. *Weather and Forecasting*, *23*(1), 3–16. https://doi.org/10.1175/2007WAF2006111.1

Maneesha, K., Murty, V. S., Ravichandran, M., Lee, T., Yu, W., & McPhaden, M. (2012). Upper ocean variability in the Bay of Bengal during the tropical cyclones Nargis and Laila. *Progress in Oceanography*, *106*, 49–61. https://doi.org/10.1016/j.pocean.2012.06.006

Mann, M. E., & Emanuel, K. A. (2006). Atlantic hurricane trends linked to climate change. *Eos, Transactions American Geophysical Union*, *87*(24), 233–241. Eos (Washington, D.C.). https://doi.org/10.1029/2006EO240001

McDougall, T. J., & Barker, P. M. (2011). *Getting started with TEOS-10 and the Gibbs Seawater (GSW) oceanographic toolbox* (p. 28). SCOR/IAPSO WG127.

Mei, W., Lien, C.-C., Lin, I.-I., & Xie, S.-P. (2015). Tropical cyclone–induced ocean response: A comparative study of the South China Sea and tropical Northwest Pacific. *Journal of Climate*, *28*(15), 5952–5968. https://doi.org/10.1175/JCLI-D-14-00651.1

Mei, W., & Pasquero, C. (2013). Spatial and temporal characterization of sea surface temperature response to tropical cyclones. *Journal of Climate*, *26*(11), 3745–3765. https://doi.org/10.1175/JCLI-D-12-00125.1

Mei, W., Primeau, F., McWilliams, J. C., & Pasquero, C. (2013). Sea surface height evidence for long-term warming effects of tropical cyclones on the ocean. *Proceedings of the National Academy of Sciences of the United States of America*, *110*(38), 15207–15210. https://doi.org/10.1073/pnas.1306753110

Neetu, S., Lengaigne, M., Vincent, E. M., Vialard, J., Madec, G., Samson, G., et al. (2012). Influence of upper-ocean stratification on tropical cyclone-induced surface cooling in the Bay of Bengal. *Journal of Geophysical Research*, *117*(C12). https://doi.org/10.1029/2012JC008433

Ni, Z., Yu, J., Shang, X., Jin, W., Luo, Y., Vetter, P. A., et al. (2021). Response of the upper ocean to tropical cyclone in the Northwest Pacific observed by gliders during fall 2018. *Acta Oceanologica Sinica*, *40*(1), 103–112. https://doi.org/10.1007/s13131-020-1672-3

Park, J., Yeo, D., Lee, K., Lee, H., Lee, S., Noh, S., et al. (2019). Rapid decay of slowly moving Typhoon Soulik (2018) due to interactions with the strongly stratified Northern East China Sea. *Geophysical Research Letters*, *46*(24), 14595–14603. https://doi.org/10.1029/2019GL086274

Park, J. J., Kwon, Y.-O., & Price, J. F. (2011). Argo array observation of ocean heat content changes induced by tropical cyclones in the north Pacific. *Journal of Geophysical Research*, *116*(C12), C12025. https://doi.org/10.1029/2011JC007165

Pasquero, C., & Emanuel, K. (2008). Tropical cyclones and transient upper-ocean warming. *Journal of Climate*, *21*(1), 149–162. https://doi.org/10.1175/2007JCLI1550.1

Patel, R. (2023). Isothermal layer depth computation [Software]. *MATLAB Central File Exchange*. https://www.mathworks.com/matlabcentral/fileexchange/53371-isothermal-layer-depth-computation

Potter, H., Drennan, W. M., & Graber, H. C. (2017). Upper ocean cooling and air-sea fluxes under typhoons: A case study. *Journal of Geophysical Research: Oceans*, *122*(9), 7237–7252. https://doi.org/10.1002/2017JC012954

Powell, M. D., Vickery, P. J., & Reinhold, T. A. (2003). Reduced drag coefficient for high wind speeds in tropical cyclones. *Nature*, *422*(6929), 279–283. https://doi.org/10.1038/nature01481

Price, J. F. (1981). Upper ocean response to a hurricane. *Journal of Physical Oceanography*, *11*(2), 153–175. https://doi.org/10.1175/1520-0485(1981)011<0153:UORTAH>2.0.CO;2

Price, J. F., Sanford, T. B., & Forristall, G. Z. (1994). Forced stage response to a moving hurricane. *Journal of Physical Oceanography*, *24*(2), 233–260. https://doi.org/10.1175/1520-0485(1994)0242.0.CO;2

Reul, N., Chapron, B., Grodsky, S. A., Guimbard, S., Kudryavtsev, V., Foltz, G. R., & Balaguru, K. (2021). Satellite observations of the sea surface salinity response to tropical cyclones. *Geophysical Research Letters*, *48*(1). https://doi.org/10.1029/2020GL091478

Ridgway, K. R., & Godfrey, J. S. (1997). Seasonal cycle of the East Australian current. *Journal of Geophysical Research*, *102*(C10), 22921–-22936. https://doi.org/10.1029/97JC00227

Roemmich, D., Alford, M. H., Claustre, H., Johnson, K. S., King, B., Moum, J., et al. (2019). On the future of Argo: A global, full-depth, multi-disciplinary array. *Frontiers in Marine Science*, *6*. https://doi.org/10.3389/fmars.2019.00439

Sanford, T. B., Price, J. F., Girton, J. B., & Webb, D. C. (2007). Highly resolved observations and simulations of the ocean response to a hurricane. *Geophysical Research Letters*, *34*(13), L13604. https://doi.org/10.1029/2007GL029679

Scoccimarro, E., Gualdi, S., Bellucci, A., Sanna, A., Fogli, P. G., Manzini, E., et al. (2011). Effects of tropical cyclones on ocean heat transport in a high-resolution coupled general circulation model. *Journal of Climate*, *24*(16), 4368–4384. https://doi.org/10.1175/2011JCLI4104.1

Scrosati, R. A. (2020). Upwelling spike and marked SST drop after the arrival of cyclone Dorian to the Atlantic Canadian coast. *Journal of Sea Research*, *159*, 101888. https://doi.org/10.1016/j.seares.2020.101888

Sriver, R. L., Goes, M., Mann, M. E., & Keller, K. (2010). Climate response to tropical cyclone-induced ocean mixing in an Earth system model of intermediate complexity. *Journal of Geophysical Research*, *115*(C10). https://doi.org/10.1029/2010JC006106

Talley, L. D., Pickard, G. L., Emery, W. J., & Swift, J. H. (2011). *Descriptive physical oceanography an introduction* (6th ed.). Elsevier Science.

The MathWorks Inc. (2022). MATLAB version: 9.13.0 (R2022b) [Software]. *The MathWorks Inc*. Retrieved from https://www.mathworks.com

Vincent, E. M., Lengaigne, M., Vialard, J., Madec, G., Jourdain, N. C., & Masson, S. (2012). Assessing the oceanic control on the amplitude of sea surface cooling induced by tropical cyclones. *Journal of Geophysical Research*, *117*(C5). https://doi.org/10.1029/2011JC007705

Vincent, E. M., Madec, G., Lengaigne, M., Vialard, J., & Koch-Larrouy, A. (2013). Influence of tropical cyclones on sea surface temperature seasonal cycle and ocean heat transport. *Climate Dynamics*, *41*(7–8), 2019–2038. https://doi.org/10.1007/s00382-012-1556-0

21699291, 2024, 4, Downloaded from https://agupubs.onlinelibrary.wiley.com/doi/10.1029/2023JC020627, Wiley Online Library on [18/06/2024]. See the Terms and Conditions (https://onlinelibrary.wiley.com/terms-and-conditions) on Wiley Online Library for rules of use; OA articles are governed by the applicable Creative Commons License

Wang, G., Wu, L., Johnson, N. C., & Ling, Z. (2016). Observed three-dimensional structure of ocean cooling induced by Pacific tropical cyclones. *Geophysical Research Letters*, *43*(14), 7632–7638. https://doi.org/10.1002/2016GL069605

Wang, X., Wang, C., Han, G., Li, W., & Wu, X. (2014). Effects of tropical cyclones on large-scale circulation and ocean heat transport in the South China Sea. *Climate Dynamics*, *43*(12), 3351–3366. https://doi.org/10.1007/s00382-014-2109-5

Webster, P. J., Holland, G. J., Curry, J. A., & Chang, H.-R. (2005). Changes in tropical cyclone number, duration, and intensity in a warming environment. *Science*, *309*(5742), 1844–1846. https://doi.org/10.1126/science.1116448

Wentz, F. J., Gentemann, C., Smith, D., & Chelton, D. (2000). Satellite measurements of sea surface temperature through clouds. *Science*, *288*(5467), 847–850. https://doi.org/10.1126/science.288.5467.847

Wu, C.-C., Lee, C.-Y., & Lin, I.-I. (2007). The effect of the ocean eddy on tropical cyclone intensity. *Journal of the Atmospheric Sciences*, *64*(10), 3562–3578. https://doi.org/10.1175/JAS4051.1

Yan, Y., Li, L., & Wang, C. (2017). The effects of oceanic barrier layer on the upper ocean response to tropical cyclones. *Journal of Geophysical Research: Oceans*, *122*(6), 4829–4844. https://doi.org/10.1002/2017JC012694

Yang, B., Hou, Y., Hu, P., Liu, Z., & Liu, Y. (2015). Shallow ocean response to tropical cyclones observed on the continental shelf of the northwestern South China Sea. *Journal of Geophysical Research: Oceans*, *120*(5), 3817–3836. https://doi.org/10.1002/2015JC010783

Yang, Y. J., Chang, M.-H., Hsieh, C.-Y., Chang, H.-I., Jan, S., & Wei, C.-L. (2019). The role of enhanced velocity shears in rapid ocean cooling during Super Typhoon Nepartak 2016. *Nature Communications*, *10*(1), 1627. https://doi.org/10.1038/s41467-019-09574-3

Zedler, S. E., Dickey, T. D., Doney, S. C., Price, J. F., Yu, X., & Mellor, G. L. (2002). Analyses and simulations of the upper ocean's response to Hurricane Felix at the Bermuda Testbed Mooring site: 13–23 August 1995. *Journal of Geophysical Research*, *107*(C12), 25-1–25-29. https://doi.org/10.1029/2001JC000969

Zedler, S. E., Niiler, P. P., Stammer, D., Terrill, E., & Morzel, J. (2009). Ocean's response to Hurricane Frances and its implications for drag coefficient parameterization at high wind speeds. *Journal of Geophysical Research*, *114*(C4), C04016. https://doi.org/10.1029/2008JC005205

Zhang, H. (2023). Modulation of upper ocean vertical temperature structure and heat content by a fast-moving tropical cyclone. *Journal of Physical Oceanography*, *53*(2), 493–508. https://doi.org/10.1175/JPO-D-22-0132.1

Zhang, H., Chen, D., Zhou, L., Liu, X., Ding, T., & Zhou, B. (2016). Upper ocean response to typhoon Kalmaegi (2014). *Journal of Geophysical Research: Oceans*, *121*(8), 6520–6535. https://doi.org/10.1002/2016JC012064

Zhang, H., He, H., Zhang, W.-Z., & Tian, D. (2021). Upper ocean response to tropical cyclones: A review. *Geoscience Letters*, *8*(1), 1–12. https://doi.org/10.1186/s40562-020-00170-8

Zhang, H., Liu, X., Wu, R., Liu, F., Yu, L., Shang, X., et al. (2019). Ocean response to successive typhoons Sarika and Haima (2016) based on data acquired via multiple satellites and moored array. *Remote Sensing*, *11*(20), 2360. https://doi.org/10.3390/rs11202360

Zhang, H., Wu, R., Chen, D., Liu, X., He, H., Tang, Y., et al. (2018). Net modulation of upper ocean thermal structure by typhoon Kalmaegi (2014). *Journal of Geophysical Research: Oceans*, *123*(10), 7154–7171. https://doi.org/10.1029/2018JC014119

Zhang, J., Lin, Y., Chavas, D. R., & Mei, W. (2019). Tropical cyclone cold wake size and its applications to power dissipation and ocean heat uptake estimates. *Geophysical Research Letters*, *46*(16), 10177–10185. https://doi.org/10.1029/2019gl083783

Zheng, Z.-W., Ho, C.-R., & Kuo, N.-J. (2008). Importance of pre-existing oceanic conditions to upper ocean response induced by Super Typhoon Hai-Tang. *Geophysical Research Letters*, *35*(20), L20603. https://doi.org/10.1029/2008GL035524

Zhu, T., & Zhang, D.-L. (2006). The impact of the storm-induced SST cooling on hurricane intensity. *Advances in Atmospheric Sciences*, *23*(1), 14–22. https://doi.org/10.1007/s00376-006-0002-9

21699291, 2024, 4, Downloaded from https://agupubs.onlinelibrary.wiley.com/doi/10.1029/2023JC020627, Wiley Online Library on [18/06/2024]. See the Terms and Conditions (https://onlinelibrary.wiley.com/terms-and-conditions) on Wiley Online Library for rules of use; OA articles are governed by the applicable Creative Commons License